Effects of chiral dopants on double-twist configurations of lyotropic chromonic liquid crystals in a cylindrical cavity

Jonghee Eun,[1] Sung-Jo Kim,[2,*] and Joonwoo Jeong[1,2,†]
[1]*Department of Physics, Ulsan National Institute of Science and Technology, Ulsan, Republic of Korea*
[2]*Center for Soft and Living Matter, Institute for Basic Science, Ulsan, Republic of Korea*

(Received 22 April 2019; published 9 July 2019)

We investigate how chiral dopants affect the chiral symmetry breaking of lyotropic chromonic liquid crystals (LCLCs) focusing on the double-twist (DT) director configurations in a cylindrical capillary. LCLCs of unusual elastic properties tend to exhibit chiral director configurations under confinement despite the absence of intrinsic chirality. The DT director configuration in a cylindrical cavity with a degenerate planar anchoring, resulting from the large saddle-splay-to-twist elastic modulus ratio, is a representative example. Here we start by reexamining the DT configuration of nematic disodium cromoglycate in a cylindrical capillary and estimate the ratio of saddle splay to bend modulus $K_{24}/K_3 = 0.5\pm0.1$. Additionally, we study the DT configurations of the chiral nematic LCLCs with chiral dopants. The DT configuration becomes homochiral when the dopant concentration surpasses the critical concentration. We characterize these chiral DT configurations and provide a theoretical model on their energetics. Finally, we observe how the enantiomeric excess of chiral dopants determines the director configuration when dopants of two different handednesses are mixed.

DOI: 10.1103/PhysRevE.100.012702

I. INTRODUCTION

Understanding chiral nematic liquid crystals (LCs) under confinement has been of vital interest as well as essential to the development of practical applications such as LC lasers and thermometers [1–3]. The twisted structures of the chiral nematic LCs are often incommensurate with the geometry, dimension, and surface anchoring of the confinement. Namely, the confined chiral nematic LCs struggle to retain their given helical pitch and the preferred directors at the confining wall. Thus they often exhibit intriguing frustrated director configurations with topological defects, e.g., skyrmions in slit cells with the cell gap comparable to the helical pitch [4–12]. Besides the planar slit or wedge cell, spherical droplets and cylindrical cavities with curved surfaces have been popular confining geometries for the chiral nematic LCs [13–26].

Nematic lyotropic chromonic LCs (LCLCs) often present twisted director configurations, despite the absence of chiral nature. Unusual elastic properties of the LCLCs, i.e., the small twist elastic modulus K_2 compared to other moduli and large saddle-splay elastic modulus K_{24} compared to the K_2, are responsible for the spontaneous chiral symmetry breaking to lower the total elastic free energy [18,27–34]. For example, the double twist, also known as escaped twist, director configuration of LCLCs in a cylindrical cavity is the archetypal example of how the K_{24} and the deviatoric curvatures of the confining wall break chiral symmetry [29,30]. Note that the confinement-induced twist in LCLCs can be either right or left handed with the same probability, which often gives rise to domain-wall-like topological defects. In contrast, a chiral nematic LC possesses a specific handedness imposed by its intrinsic chirality or the extrinsic chirality of chiral dopants added.

Chiral nematic LCLCs also have been of primary interest. The water-soluble chiral dopants such as chiral amino acids and sugars have been identified, and their helical twisting powers have been measured [18,19,23,25,26,35,36]. Because there exist two origins of twist deformations, i.e., confinement-induced and dopant-induced ones, their combination may lead to intriguing behaviors. For instance, chirality amplification by chiral additives has been reported in tactoids of LCLCs, and this provides confined LCLCs with potential as biosensors. Similar phenomena may arise in other confining geometries such as spherical droplets, capillaries, and cylindrical shells [28–34]. Especially, because LCLCs having unprecedentedly large K_{24} provide a unique platform to study the saddle-splay-induced chiral symmetry breaking under confinement, it would be intriguing to see the interplay of chiral dopants' helical twisting power and K_{24} in the symmetry breaking. It seems that the elusive and possibly small K_{24}s of most thermotropic LCs [37,38] have precluded this kind of study.

Here we report the experimental and theoretical study of the director configurations of achiral and chiral nematic LCLCs in a cylindrical cavity with a planar degenerate anchoring. The first significance of this work is that we present advanced investigations of the achiral nematic LCLCs in cylinders compared to the previous works [29,30]; we measure DSCG's K_{24} considering the energy-minimizing director configuration, not assuming a linear twist. More importantly, we elucidate the subtle interplay of K_{24} and the helical twisting power imposed by chiral dopants. The cylindrical geometry, the chiral nematic LCLCs (CLCLCs) of $K_{24} > 2K_2$,

*Present address: Department of Physics, Ulsan National Institute of Science and Technology, Ulsan, Republic of Korea.
†jjeong@unist.ac.kr

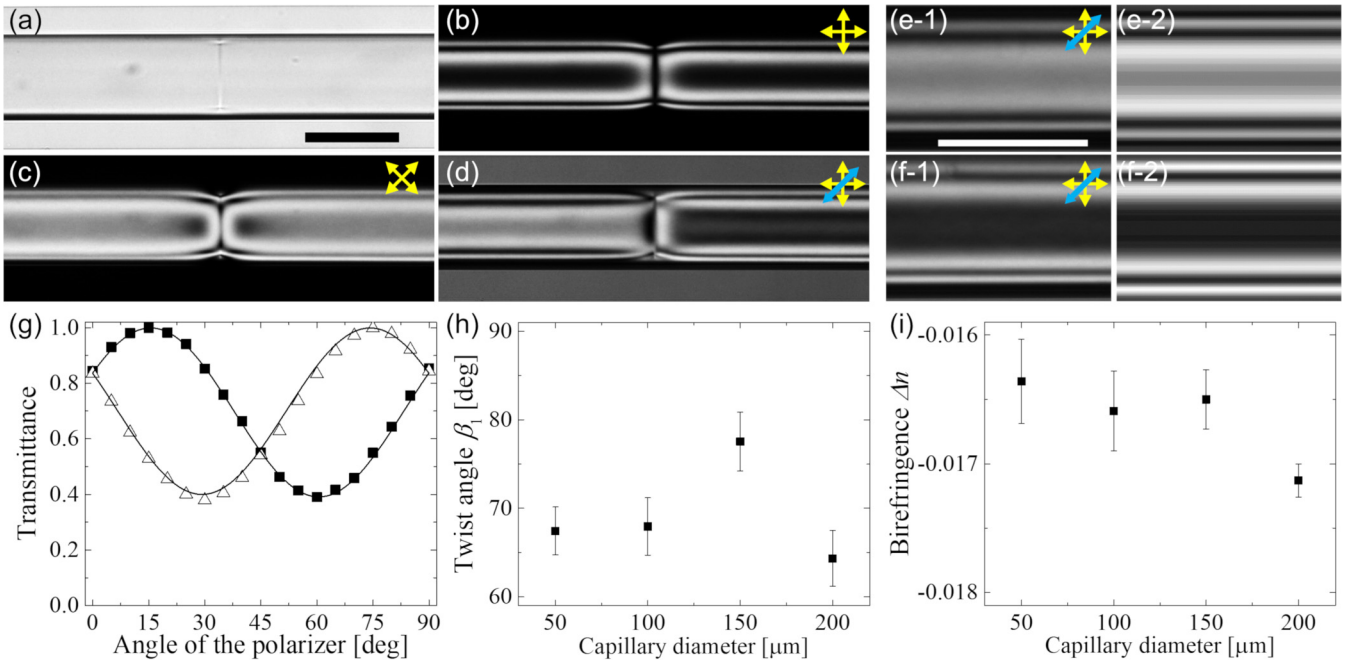

FIG. 1. Optical microscopy of 14.0% (wt/wt) nematic disodium cromoglycate (DSCG) confined inside a cylindrical cavity of 100-μm diameter and characterization of the DT configuration. Scale bar is 100 μm. (a) Bright-field and [(b) and (c)] POM images of the confined DSCG between crossed polarizers of which pass axes are shown as yellow double arrows. (d) A POM image of the same DSCG between crossed polarizers with a full wave plate of 550-nm retardance inserted before the analyzer. A blue single arrow represents the slow axis of the wave plate. Note that all the images are taken under a quasimonochromatic illumination of 660 nm wavelength. The discontinuity in the brightness pattern at the center corresponds to the domain-wall-like defect. (e) and (f) Representative experimental POM images of the domains of different handedness (see e-1 and f-1) and corresponding POM patterns simulated by Jones calculus (see e-2 and f-2). Note that the wave plate distinguishes the difference in handedness as in (d). The handedness of the DT configuration in (e) and (f) are right and left handed, respectively. (See Fig. 2 for the schematic diagram of the director configuration.) (g) The transmittance of the 660-nm illumination through the center of the cylinder as a function of the angle of the polarizer (see Materials and Methods), The intensities are measured from rectangles spanning the 10% of the cylinder diameter at the center of the cylinder. Filled and empty symbols are experimental data from the right-handed domain shown in (e) and the left-handed one shown in (f), respectively. The solid lines are the best matching numerical calculation data. (h) and (i) The twist angle β_1 and birefringence Δn of the DT configuration of 14.0% (wt/wt) nematic DSCG in capillaries of different diameters. Each data point is the average value of 10 different measurements, and the error bar represents the standard deviation.

and well-defined helical pitches enable us to observed the interplay. Specifically, because of the deviatoric curvature of the cylinder, i.e., the difference in the curvatures along the circumference and the capillary axis, the large K_{24} of LCLCs induces a spontaneous twist deformation resulting in the double-twist (DT) configuration. In addition to this confinement-induced twist, CLCLCs also want to have the DT configuration with their helical pitches, which can be incommensurate with the K_{24} effect. For instance, the saddle-splay energy minimizes when the surface directors align along the circumference while a particular helical pitch wants the surface directors to align along the cylindrical axis. We investigate the director configurations of CLCLCs in a cylindrical cavity varying the concentration of chiral dopant. We also characterize the director configuration and identify the critical dopant concentration for the chirality amplification, i.e., the defect-free mono-domain formation. Lastly, we confirm that the enantiomeric excess of mixed chiral dopants determines the handedness of the director configuration.

We adopt aqueous disodium cromoglycate (DSCG) solution as a model system, which is used as an anti-inflammatory agent to treat diseases such as asthma. Charged and planklike DSCG molecules form elongated aggregates by stacking in water via noncovalent attractions, and the aggregates align to exhibit liquid crystalline phases according to the temperature and concentration. Its phase diagram, viscoelastic properties, and chiral dopants have been investigated [18,19,23,25,26,35,36,39,40], and the saddle-splay-induced chiral symmetry breaking has been reported with an approximate measurement of K_{24}/K_3 [30].

II. RESULTS AND DISCUSSION

A. Achiral nematic LCLCs in a cylindrical cavity

Nematic LCLCs of large saddle-splay elastic moduli K_{24} exhibit the double-twist (DT) configuration in a cylindrical cavity with a degenerate planar anchoring. Figure 1 shows the polarized optical microscopy (POM) images of nematic disodium cromoglycate (DSCG) confined in a glass capillary of 100 μm in diameter. The symmetric texture about the capillary axis and nondarkness of the central region under crossed polarizers hint at an azimuthally symmetric but twisted director configuration. Although the LCLCs are achiral intrinsically, the K_{24} greater than two times the twist modulus K_2 induces spontaneous chiral symmetry breaking [29,30]. K_{24} can lower total elastic free energy by aligning the

surface directors at the cavity wall along the circumference, i.e., the direction of the highest curvature [29,30,41].

The directors twist along the cylinder radius in a nonlinear manner according to K_2/K_3 and K_{24}/K_3 where K_3 is the bend elastic modulus [29]. We adopt the DT director configuration $\mathbf{n} = -\sin\beta(r)\hat{\phi} + \cos\beta(r)\hat{\mathbf{z}}$ in cylindrical coordinates, where $\beta(r)$ describes how the directors twist along the radius of the cylinder. Elastic free energy minimization using the Euler-Lagrange method gives the energy-minimizing Eq. (1) [29].

$$\beta(r) = \arctan \frac{2\sqrt{K_2 K_{24}(K_{24} - 2K_2)}\, r/R}{\sqrt{K_3}[K_{24} - (K_{24} - 2K_2) r^2/R^2]}. \quad (1)$$

Equation (1) describes how the director twist along the cylinder radius r according to the elastic moduli; note that the DT configuration arises only when $K_{24} > 2K_2$ and the splay deformation of the modulus K_1 does not participate in the DT configuration. This nonlinear twist profile makes it difficult to characterize the degree of twist in the DT director configuration unless the directors are visible [29] or the specimen is in the wave-guiding regime [30]. Because of a small birefringence Δn of approximately -0.02, our model system, i.e., nematic DSCG in 100-μm diameter capillaries, neither allow the visualization of the director field from the flickering nor lies in the wave-guiding regime.

We estimate the twist angle at the capillary wall and the K_{24} by comparing experimentally measured transmittance profiles with Jones calculus-simulated profiles. Once the twist angle at the capillary wall of radius R, i.e., $\beta_1 = \beta(r = R)$, is measured, we can estimate K_{24} according to Eq. (1) [29]; $\tan\beta_1 = \sqrt{\frac{K_{24}(K_{24}-2K_2)}{K_2 K_3}}$. The average twist angle β_1, measured from 10 different regions in five different capillaries is 68±3 deg which corresponds to $K_{24}/K_3 = 0.5\pm0.1$ when we assume $K_2/K_3 = 1/30$ of 14.0% (wt/wt) nematic DSCG at 21.5 °C [39]. In principle, β_1 should be independent of the size of the capillary, and we investigate this in the range of 50–200 μm in diameter as shown in Fig. 1(h). Although there are unexpected increases of β_1 at 150-μm diameter and $|\Delta n|$ at 200-μm diameter, the data shows no explicit size dependency of the DT configuration as expected in the theoretical calculation. We presume the deviations may result from the unavoidable evaporation of water out of the nematic DSCG during the capillary injection. The evaporation results in the increase of the concentration and the changes of elastic moduli. Additionally, some flow-induced alignment despite the injection in the isotropic phase, or anisotropy at the capillary wall, which was not captured by atomic force microscopy [29], may contribute to the deviations. These need further investigations. Note that our $K_{24}/K_3 = 0.5\pm0.1$ of DSCG is different from the one in Nayani *et al.* because they assume a linear twist along the radius [30].

For this estimation, we experimentally measure the transmittance of a quasimonochromatic illumination (λ = 660 nm, FWHM = 25 nm) through the central region of a capillary while simultaneously rotating a polarizer and an analyzer in the opposite direction (see Materials and Methods). We compare this transmittance profile to numerically generated profiles. For the numerical calculation, adopting the experimentally measured diameters of capillaries, we generate Jones-matrix-calculated transmittance profiles through the DT configurations of various β_1 and Δn. Specifically, with $K_2/K_3 = 1/30$, we vary β_1 from 40 to 88 deg by 1 deg and Δn from -0.0200 to -0.0160 by 0.0001. Utilizing Eq. (1) as the director profile and the experimentally measured diameters of capillaries, we find the β_1 and Δn that best match experimental data based on the least-square method. To resolve the degeneracy issue that different director profiles may lead to the same transmittance profile, we double-check the results by the comparison of experimental POM images with the Jones matrix-calculated POM images. Figures 1(e) and 1(f) show the representative experimental data and the corresponding numerical calculation results.

Domains of right or left handedness both appear with the same probability because achiral LCLCs do not have a preferred handedness for the twist. As shown in Fig. 1(d), the POM images with a full wave plate inserted in front of the analyzer clearly distinguish domains of different handednesses. Note also that there exists a domain-wall-like defect between two domains of different handednesses. To estimate the probability of each handedness, we measure the total lengths of the domains of each handedness and divide them by the total length of all domains. As shown in the far-left data point of Fig. 3(e), we confirm that the handedness ratio for the neat DSCG, i.e., with no dopant added, is close to 1:1 and the achiral DSCG does not have a preferred handedness. The data point is the average of measurements in six different capillaries of ∼4 cm in length, and the standard deviation is shown as an error bar.

B. Chiral nematic LCLCs in a cylindrical cavity

Inspired by this chiral symmetry breaking of the achiral LCLCs, we investigate chiral nematic LCLCs (CLCLCs) with the amino acid, L-alanine, as a chiral dopant [19,23,25,26,35,36]. With the same degenerate planar anchoring in a cylindrical cavity, CLCLCs also give the DT configuration but of a preferred handedness. As shown in Figs. 2(a)–2(d), the CLCLCs form a homochiral monodomain without a defect when the concentration of a chiral dopant surpasses a critical concentration, ∼0.1% (wt/wt) of L-alanine. It is noteworthy that the opposite handednesses induced by L-alanine and D-alanine are manifested in their different textures under crossed polarizer and the wave plate [Compare Figs. 2(a-2) and 2(b-2)]. Additionally, the different appearance in Fig. 2(d) by Sunset Yellow FCF (SSY) results from its large $|\Delta n|$ and β_1 compared to the ones in DSCG. Figures 2(e) and 2(f) show the schematic diagram of the DT configuration of the left and right handedness, respectively. The L-alanine induces the left-handed twist [19], i.e, Fig. 2(e). When the concentration is much greater than the critical concentration, e.g., 5.0% (wt/wt) L-alanine, the well-known fingerprint texture of chiral nematic LCs appears as expected [19,23,25,36]. To elaborate on combined roles of chiral dopants and the large K_{24}, here, we focus on the low dopant concentration regime where the twist angle β_1 is smaller than $\pi/2$, so there exist no half-pitch lines, so-called fingerprint.

The critical concentration of the chiral dopant for the homochiral monodomain is manifested in the formation of the nematic domains after lowering the sample temperature

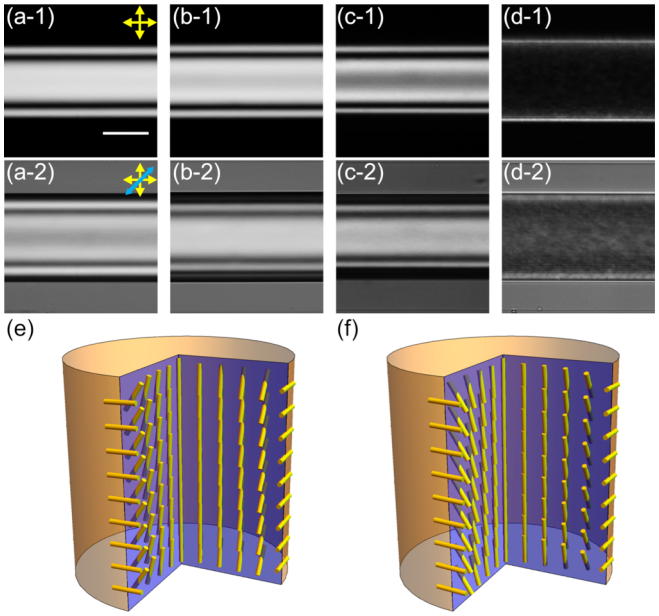

FIG. 2. Homochiral DT configurations of CLCLCs with different chiral dopants and the corresponding POM texture in cylindrical cavities. The yellow double arrows represent the pass axes of crossed polarizers, and the blue arrow represents the slow axis of the full wave plate. The scale bar is 50 μm. (a-1)–(d-1) The POM images under crossed polarizers with no wave plate, and the POM images of (a-2)–(d-2) are taken with a full wave plate inserted before the analyzer. (a) 14.0% (wt/wt) DSCG + 2.0% (wt/wt) L-alanine, (b) 14.0% (wt/wt) DSCG + 2.0% (wt/wt) D-alanine, (c) 14.0% (wt/wt) DSCG + 2.0% (wt/wt) D-glucose, (d) 30.0% (wt/wt) Sunset Yellow (SSY) + 0.1% (wt/wt) Brucine sulfate heptahydrate. (e) and (f) Schematic diagrams of the DT configurations. The yellow rods represent the nematic directors. According to the right-hand rule, the director configuration in (e) is left handed, and the one in (f) is right handed. Namely, in the right-handed one in (f), the tip of the director rotates clockwise as the director proceeds radially.

from isotropic to nematic phase. As shown in Fig. 3, the nematic texture of doped DSCG with the low concentration of L-alanine, i.e., $\leqslant$0.1% (wt/wt), including the neat DSCG, appear inhomogeneous because two handednesses coexist right after the samples reach the fully nematic phase. In contrast, CLCLCs with more than 0.1% (wt/wt) of L-alanine exhibit defect-free monodomains. To our interest, the DSCG with 0.1% (wt/wt) of L-alanine forms the monodomain only after 1 h, while the specimens with the lower concentration of L-alanine retain domains of both handednesses up to 24 h. This result advises that 0.1% (wt/wt) L-alanine is close to the critical concentration for the monodomain formation.

If the dopant concentration is smaller than the critical value, domains of different handednesses still exist with defects between them, but one handedness appears with a higher probability. As mentioned earlier, we define the probability of a certain handedness by the share of the corresponding domains in the whole sample, i.e., the summed length of the one-dimensional domains divided by the total length of the sample. Figure 3(e) shows the probabilities of each handedness from chiral DSCG with L-alanine as a chiral dopant. We notice that the critical concentration is close to 0.1% (wt/wt), which is consistent with the observation in Figs. 3(a)–3(d). In Fig. 3(e), it is noteworthy that we measure the lengths after 24 h from the preparation of the samples; after 24 h from the preparation, the merging dynamics and the ratio change becomes slow. Because domains disappear and merge during the relaxation accompanying the annihilation of the defects separating them, the ratio may depend on the moment of the measurement. Lastly, we specify that the measurement in Fig. 3(e) is performed only in 100-μm diameter and the merging dynamics may show the size dependence.

We propose that the critical concentration of the chiral dopant for the monodomain formation can be understood by a comparison between an average distance between dopant molecules and a correlation distance between LCLCs aggregates [42,43]. Under the assumption of uniformly dispersed dopant molecules, the average distance between the dopant molecules is approximately the diameter of a spherical volume taken by a single dopant molecule on average; for 0.1% (wt/wt) of L-alanine, the distance is of the order of 10 nm. If this distance is comparable or shorter than a correlation length over which the motions of LCLCs' aggregates are correlated, twist deformation induced by the dopant molecules may propagate over the whole sample in a coherent manner. Otherwise, despite the existence of chiral dopant molecules of one handedness, the nematic phase may exhibit domains of different handednesses. To our knowledge, the correlation length of aggregates in nematic DSCG around the room temperature has not been estimated but the correlation length of another well-known LCLC, SSY, is known to be about 8 nm [44]. This is similar to the average molecule-molecule distance of L-alanine at 0.1% (wt/wt). Presuming the correlation length of the DSCG aggregates is of the same order of the correlation length of SSY aggregates, we suppose it is reasonable that the critical L-alanine concentration is of the order of 0.1% (wt/wt). We hope this argument for the critical dopant concentration can be confirmed in different experimental conditions having a wide range of the correlation lengths, e.g., different LCLCs at various temperatures and concentrations.

To investigate quantitatively how the chiral dopants affect the director configuration, we estimate the twist angles β_1s of the DT configuration of chiral nematic DSCG. As in the case without chiral dopants, we experimentally measure the transmittance of quasimonochromatic illumination through the central regions of the capillaries while rotating the polarizer and analyzer. Then the transmittance profiles are compared to the numerically generated profiles to find the best matching Δn and β_1. Note we assume that, at a low concentration of chiral dopants, the DT configuration is not much deviated from Eq. (1) with the same $K_2/K_3 = 1/30$. The empty symbols in Fig. 4 summarize the results. While $|\Delta n|$ increases as the dopant concentration increases, we find no strong dependence of the twist angle β_1 on the dopant concentration. β_1s range between 65 and 75 deg while we vary the dopant concentration from 0% to 1.0% (wt/wt). Note that the twist angles of L-alanine-doped and D-alanine-doped DSCG only differ in their signs, i.e., the handedness; Fig. 2 demonstrates that the crossed polarizers hardly distinguish them but the wave plate can.

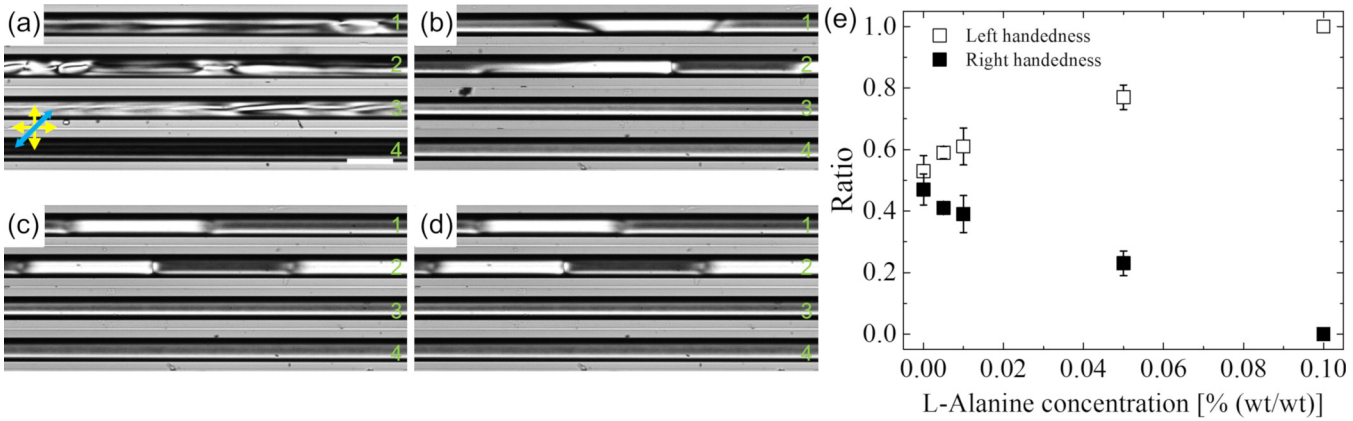

FIG. 3. The characterization of the critical concentration of L-alanine for the homochiral mono-domain formation. (a)–(d) The POM images of the DT configuration with different concentrations of L-alanine after the phase transition from the isotropic to nematic phase. The number on each capillary specifies a different concentration of L-alanine: (1) 0, (2) 0.01, (3) 0.1, and (4) 0.3% (wt/wt). (a) 0 h, (b) 1 h, (c) 3 h, and (d) 24 h after reaching the nematic phase at 21.5 °C. The yellow double arrows represent the pass axes of the crossed polarizer, and the blue single arrow is the slow axis of the wave plate. The scale bar is 200 μm. (e) The length ratio of the domains of two different handednesses. The empty and filled symbols are the length ratios of the left- and right-handed domains, respectively. Each data point is the average of six different measurements, and the standard deviation is shown as the error bar.

Numerical calculations on the DT configuration of CLCLCs with a large K_{24} support this weak dependence of the twist angle on the dopant concentration. Because the helical twisting power of the chiral dopant, L-alanine, is reported [19,23,26,35,36], we estimate the helical pitches from the dopant concentrations. Considering the helical pitch and K_{24}, we calculate the director configuration of CLCLCs in a cylindrical cavity with degenerate planar anchoring [14,16]. The Euler-Lagrange equation from the Oseen-Frank elastic free energy becomes

$$s^2\frac{d^2\beta(s)}{ds^2}+s\frac{d\beta(s)}{ds}-\frac{1}{2}\sin 2\beta(s)\cos 2\beta(s) - \frac{2\sin^3\beta(s)\cos\beta(s)}{K_2/K_3}+s\,q_0(\cos 2\beta(s)-1)=0, \quad (2)$$

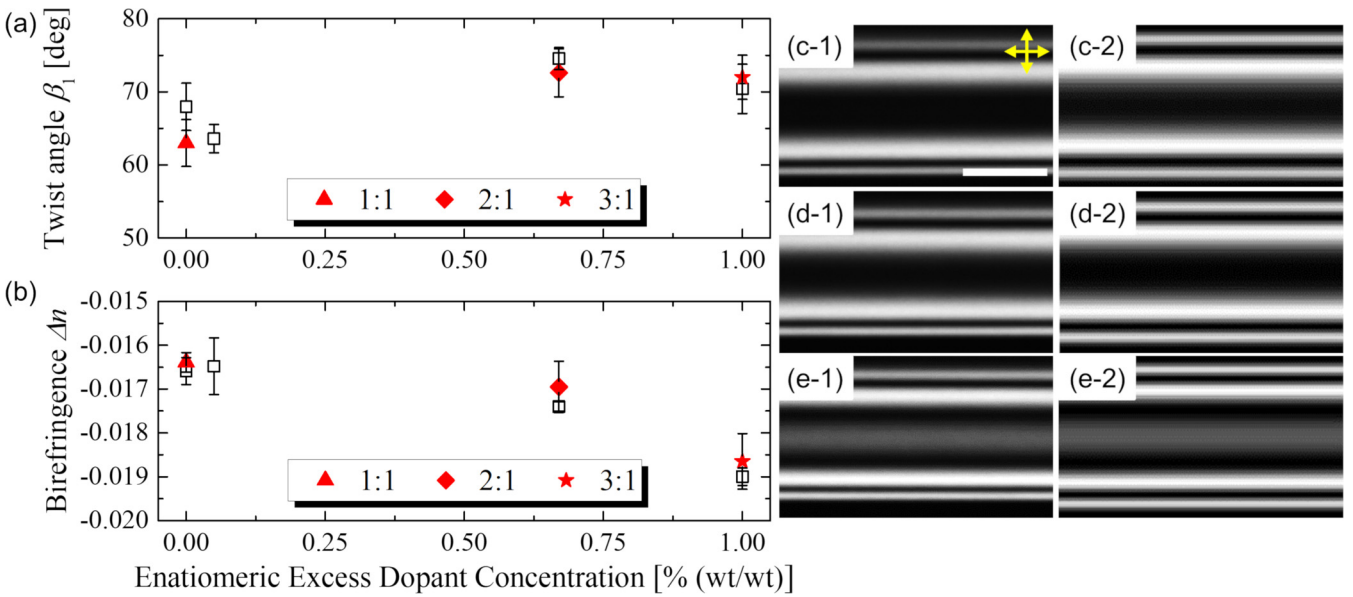

FIG. 4. The twist angle, birefringence, POM images, and corresponding simulated optical textures of the DT configuration of 14.0% (wt/wt) DSCG in a cylinder, according to the concentration of L-alanine and D-alanine. (a) The dependence of the twist angle β_1 on the (excess) dopant concentration. (b) The dependence of the birefringence Δn on the (excess) dopant concentration. In (a) and (b), the empty symbols are measured when only L-alanine is added. The filled symbols represent the excess concentrations of L-alanine in the mixture of L- and D-alanine, according to the mixture ratio (L-alanine:D-alanine) shown in the legend. (c)–(e) The POM images (the left column) and corresponding Jones-calculus-simulated optical textures (the right column) according to the concentration of L-alanine: (c) 0, (d) 0.67, and (e) 1.0% (wt/wt), respectively. The yellow double arrows indicate the pass axes of crossed polarizers. The scale bar is 50 μm.

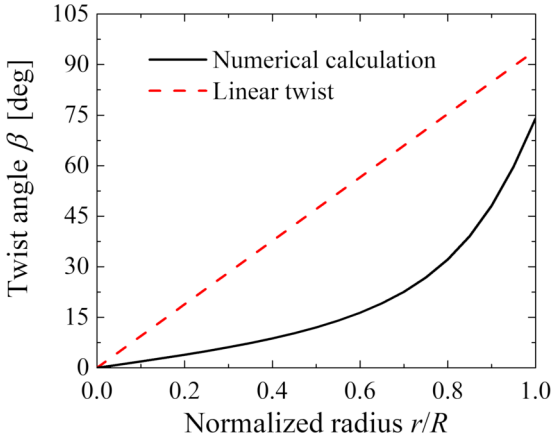

FIG. 5. An example of a numerically calculated twist angle profile $\beta(r)$ in the cylindrical capillary. The twist angle β_1 is plotted as a function of the normalized radius r/R. Here, a CLCLC with a 191-μm helical pitch is confined in a 100 μm-diameter capillary. The profile of a linear twist is shown as the red dashed line, and its twist angle at the capillary wall $\beta_1 = \beta(r/R = 1)$ is 94.2 deg. The numerically calculated profile of the lowest elastic free energy follows the black solid line with $\beta_1 = 74.0$ deg.

where s is the normalized radius r/R and q_0 is $2\pi/p_0$ when p_0 is the natural pitch imposed by the chiral dopant. The boundary conditions are $\beta(s=0) = 0$ by symmetry and $\frac{d\beta(s)}{ds}|_{s=1} = \frac{K_{24}-K_2}{2K_2}\sin 2\beta(s=1) + q_0$. Assuming that the elastic moduli including K_{24} are negligibly affected by the low concentration of dopants, i.e., adapting Ks of neat nematic DSCG, we solve this differential equation numerically using the shooting method to find the total elastic free energy-minimizing DT configuration with a given helical pitch p_0. Figure 5 is one example of this calculation. A naive calculation assuming a linear twist deformation along the radius predicts the twist angle $\beta_1 = 94.2$ deg in 100-μm-diameter capillary when L-alanine concentration is 0.67% (wt/wt), because the helical pitch is 191 μm. The reported helical twisting power is $0.78 \pm 0.02 \times 10^{-2}/(\text{wt\%} * \mu\text{m})$ at 22 °C [25]. But the corresponding β_1 from our experiments is 75±1.5 deg, which shows a reasonable agreement with the numerical calculation 74.0 deg. For the case of 1.0% (wt/wt), the linear twist with a helical pitch 128 μm predicts $\beta_1 = 140.6$ deg but the experimental β_1 is only 70±3.4 deg, and the numerical calculation gives $\beta_1 = 76.5$ deg. These manifest the weak dependence of the twist angle on the dopant concentration.

The large K_3 and K_{24} compared to K_2 of LCLCs are responsible for this weak dependence of the β_1 on the dopant concentration. First, as shown in Fig. 5, the directors twist nonlinearly along the radius of the capillary. The twist angle increases slowly at a small radius because small K_2/K_3 can lower the total elastic free energy by avoiding tight bending with a small radius of curvature. More importantly, large K_{24} favors the alignment of surface directors along the circumference of the capillary, i.e., the direction along the highest curvature [29]. In other words, K_{24} makes the β_1 as close to $\frac{\pi}{2}(2n-1)$ as possible where n is an integer. Our experimental observation in Fig. 4(a) supports that β_1 is smaller than $\pi/2$ even though $p_0/4$ is greater than R.

We also confirm that enantiomeric excesses of mixed chiral dopants of different handednesses determine the DT configurations. First, we observe the DT configuration of nematic DSCG doped with the same amount of L-alanine and D-alanine; the total concentration of the dopants is 2.0% (wt/wt). This sample seems as if it does not contain any chiral dopants. Namely, as shown in Fig. 4, domains of different handednesses appear with defects between them, and β_1 is measured to be similar to the twist angle of the DT configuration without dopants. It seems that the helical twisting powers of two dopants cancel out each other. To investigate this phenomenon further, we vary the ratio of L-alanine to D-alanine while retaining the total concentration of dopants as 2.0% (wt/wt). The 2:1 (L-alanine:D-alanine) case shows a homochiral DT configuration and the β_1 is similar to the β_1 of DT configuration with L-alanine 0.67% (wt/wt), which is an algebraic enantiomeric excess. We see the same thing for the 3:1 case. We also check that even POM images look almost identical (data not shown). However, note that β_1 is not sensitive to this range of dopant concentration because of the large K_3/K_2 and K_{24}/K_2 mentioned above. Additionally, our estimation of β_1 does not consider that elastic moduli of the CLCLCs can be affected by the dopants, which may not be valid at high dopant concentrations. Thus the caveat is that the comparison between β_1s should be at a semiquantitative level.

III. MATERIALS AND METHODS

A. Preparation of nematic LCLCs confined in a cylindrical cavity

Disodium cromoglycate (DSCG, a purity of ⩾95.0%), L-alanine, D-alanine, and D-glucose were purchased from Sigma-Aldrich and used as received. By dissolving these into deionized water (18.2 MΩ cm), we prepared 14.0% (wt/wt) nematic DSCG solutions with chiral dopants; the dopant concentrations ranged from 0.005% to 5.0% (wt/wt). Sunset yellow FCF (SSY) was purchased from Sigma-Aldrich at a purity of ⩾90.0%, and it was further purified according to a published method [44]. Brucine sulfate heptahydrate also purchased from Sigma-Aldrich was used as a chiral dopant for 30.0% (wt/wt) nematic SSY solutions [22], and its concentration varied between 0.1% and 0.5% (wt/wt).

Cylindrical capillaries of the diameters with ±10% were purchased from VitroCom. They were used without any surface treatment. We filled the capillaries with LCLCs solutions in their isotropic phase (65.0 °C) to minimize the effects of flow in the nematic phase. Then, we placed the filled capillaries on a glass slide and immediately sealed the ends with epoxy glue to minimize the evaporation of water. We covered the samples with coverslips, and the gap between the glass slide and coverslip was filled with index matching oil ($n = 1.474$ at 589.3 nm; Cargille Labs). We used a temperature controller (T95-PE120; Linkam Scientific Instruments) attached to the microscope and controlled the temperature of the samples at the rate of 2.0 °C/min. All measurements were performed at 21.5 °C.

B. Optical microscopy

We collected bright-field (BF) and polarized optical microscopy (POM) images using an upright microscope

(Olympus BX53-P) with a 20× dry objective with a coverslip-thickness correction. We also used 4× and 10× dry objectives for large field-of-view images. All images were taken with a color CCD camera (INFINITY3-6URC; Lumenera) under quasimonochromatic illumination (wavelength = 660 nm, FWHM = 25 nm) derived from a LED lamp (LED4D067; Thorlabs). For both DSCG and SSY, the absorbance at 660 nm is smaller than 5% [28]. Additionally, for phase retardation experiments, a full-wave plate (optical path difference = 550 nm; Olympus) was placed in front of the analyzer.

C. Jones matrix calculation and determination of twist angles

Given a nematic director field, refractive indices, an illumination wavelength, and the diameter of a cylindrical capillary, two-dimensional (2D) transmittance profiles of samples can be simulated using Jones calculus according to the directions of the polarizer and analyzer, even with a wave plate [28,31,45]. In summary, plane waves represented by a Jones vector are projected through the optical components, i.e., the polarizers and wave plate, and the volume elements (voxels) of the director field placed on a three-dimensional grid. Then, we multiply sequentially the corresponding Jones matrices of the components and the voxels along the beam path to the input Jones vector and derive transmitted intensities at each output pixel. Note that, for this calculation, we adopt a parallel ray approximation and ignore the effects of refraction, reflection, and diffraction. Thanks to a relatively small birefringence of DSCG of ~ -0.017, the modest difference in the refractive indices of the glass and the specimen, and the refractive index matching oil surrounding the capillaries, the resulting approximate calculations can provide reasonable simulations as shown in Figs. 1(e) and 1(f).

In addition to the 2D-image simulation, we can calculate the transmittance through the central region of the capillaries, where the approximations are most valid, as we change the pass axes of the polarizer and analyzer. Specifically, these calculated transmittance profiles can be compared with the experimental transmittance profiles measured under the rotation of a polarizer and an analyzer in the opposite direction. In the experiment, we initially set the capillary and the pass axes of the polarizer and analyzer parallel, and rotate the polarizer and the analyzer in the opposite direction by 5 deg, respectively. Lastly, the numerical parameters that generate the best matching profile based on the least square method determine the twist angle β_1 and the birefringence Δn. For the confirmation of the result, the corresponding 2D transmittance image can also be compared to the experimental image.

D. Numerical calculation of the double-twist director configurations

We follow the Euler-Lagrange method in Ondris-Crawford *et al.* and Davidson *et al.* to calculate the double-twist (DT) director configuration. However, to deal with the effect of chiral dopants, we use the Oseen-Frank elastic free energy density of chiral nematic phases with $\frac{1}{2}K_2(\mathbf{n}\cdot\nabla\times\mathbf{n}+\mathbf{q_0})^2$. K_2 is the twist elastic modulus, $\mathbf{n}$ is the nematic director field, and q_0 is $2\pi/p_0$ where p_0 is the helical pitch. We numerically solve the resulting Euler-Lagrange equation, Eq. (2), to find the twist angle $\beta(r)$ as a function of the radius r of the capillary. We assume $\mathbf{n} = -\sin\beta(r)\hat{\phi} + \cos\beta(r)\hat{\mathbf{z}}$. Note that the achiral nematic case with $q_0 = 0$ is analytically solvable [29]. The saddle-splay energy term is proportional to $\sin^2\beta_1$ when β_1 is the twist angle at the confining wall, i.e., $\beta(r = R)$. Because of this sinusoidal nature of the energy landscape, we find all local minima solutions of the Euler-Lagrange equation using the shooting method. Specifically, given a helical pitch and elastic moduli, we find the list of solutions of the Euler-Lagrange equation while varying the boundary condition, i.e., the first derivative of $\beta(r)$ near $r = 0$. Then, we calculate the Oseen-Frank elastic free energy per the unit cylindrical length of each solution to find the director configuration of the lowest energy.

IV. CONCLUSION

In summary, we study the DT configurations of achiral and chiral nematic LCLCs confined in a cylindrical cavity with a degenerate planar anchoring condition. First, comparing the experimental observation of the nematic DSCG's DT configuration with numerical calculations, we measure its $K_{24}/K_3 = 0.5 \pm 0.1$ when $K_2/K_3 = 1/30$ [30,39]. In the same confinement, we also study chiral nematic LCLCs with chiral dopants of different molecules, handednesses, and concentrations. We find the doped LCLCs favor a certain handedness imposed by the chiral dopant and, at a higher concentration greater than a critical concentration, the defect-free homochiral DT configurations develop. We propose two experimental methods to determine the critical concentration and a theoretical explanation on how the critical concentration is determined. We believe similar approaches are applicable to thermotropic LCs regarding the critical dopant concentration for chiral amplification. Furthermore, we estimate the twist angles β_1s depending on the concentrations of the chiral dopant, i.e., L-alanine, at a low concentration regime. To our interest, we find no strong dependence of the twist angles on the concentration because the key factor in determining the twist angle is the saddle-splay modulus K_{24} which favors the alignment of surface director along the circumference of the cylindrical confinement. Finally, we examine chiral nematic LCLCs with two chiral dopants of two different handednesses, e.g., L-alanine and D-alanine, and confirm that the enantiomeric excess plays a role as the chiral dopant.

Looking forward, we believe the chiral LCLCs with the chiral dopants may lead to stimulating experiments and applications. First, the chiral LCLC is a promising system to study the role of the K_{24} in confined chiral nematic phases. Despite a few theoretical predictions, e.g., a discontinuous increase of twist angles in confined chiral nematic LCs because of the saddle-splay energy at the surface [14,16], there has been no experimental report. LCLCs' large K_{24} and a relatively large helical pitch of tens of microns would facilitate the observation of the steplike behavior according to the chiral dopant concentrations. Additionally, we expect the chiral LCLCs confined in novel geometries, e.g., nematic tori and cylindrical shells with anisotropic principal curvatures of both signs, might lead to discoveries of uninhabited director configurations and topological defects. Lastly, we envision that deep understanding of the interactions between LCLCs and water-soluble chiral objects of chemical and biological

interests, such as proteins and nanoparticles, may contribute to the development of practical applications. For example, we show that chiral amino acids or enantiomeric excess of them can be detected easily by optical observations when the concentration exceeds 0.1% (wt/wt). If the sensitivity of the director configuration and resulting textures to additives can be improved, LCLCs have the potential to be sensors and even a separator for chiral molecules.

ACKNOWLEDGMENTS

The authors gratefully acknowledge financial support from the Korean National Research Foundation through Grants No. NRF-2015R1A2A2A01007613 and No. IBS-R020-D1. J.J. also acknowledges partial support from the 2015 Research Fund (1.150047.01) of UNIST (Ulsan National Institute of Science and Technology).

APPENDIX: DERIVATION OF EULER-LAGRANGE EQUATION OF THE DOUBLE-TWIST CHIRAL NEMATIC LCLCS IN A CYLINDRICAL CAVITY

The elastic free energy of the confined chiral nematic liquid crystals is

$$F = \int d^3x \left[\frac{1}{2}K_1(\nabla \cdot \bar{\mathbf{n}})^2 + \frac{1}{2}K_2(\bar{\mathbf{n}} \cdot \nabla \times \bar{\mathbf{n}} + q_0)^2 + \frac{1}{2}K_3(\bar{\mathbf{n}} \times \nabla \times \bar{\mathbf{n}})^2 - \frac{1}{2}K_{24}\nabla \cdot (\bar{\mathbf{n}} \times \nabla \times \bar{\mathbf{n}} + \bar{\mathbf{n}}\nabla \cdot \bar{\mathbf{n}}) \right], \tag{A1}$$

where $\bar{\mathbf{n}}$ is the nematic director. K_1, K_2, K_3, and K_{24} are the splay, twist, bend, and saddle-splay elastic constants, respectively. q_0 is $2\pi/p_0$ when p_0 is the helical pitch of the chiral nematic phase.

Using cylindrical coordinates, with the z axis along the capillary axis of symmetry, we assume

$$\bar{\mathbf{n}} = -\sin\beta(r)\hat{\boldsymbol{\phi}} + \cos\beta(r)\hat{\mathbf{z}}, \tag{A2}$$

where $\beta(r)$ is the twist angle with respect to the z axis at radius r from the center ($0 \leqslant r \leqslant R$). Note that the azimuthally symmetric director has no $\hat{\mathbf{r}}$ component. Utilizing the azimuthal symmetry and adapting the normalized radius $s = r/R$ with the cylinder radius R and $\beta(s)$ instead of $\beta(r)$, the dimension-less free energy per unit length f becomes

$$f = \frac{F}{\pi \mathrm{L} K_3} = \int_0^1 ds \left[\frac{k_2(-q_0 s + s\beta'(s) + \sin\beta(s)\cos\beta(s))^2 + \sin^4\beta(s) - k_{24} s \sin 2\beta(s)\beta'(s)}{s} \right], \tag{A3}$$

where k_2 and k_3 are K_2/K_3 and K_{24}/K_3, respectively. Note that there is no splay deformation in our ansatz.

After the expansion of the integrand and integration, f becomes

$$\begin{aligned} f = \int_0^1 ds \left[-k_2 q_0 \sin 2\beta(s) + \frac{k_2 \cos^2\beta(s)\sin^2\beta(s)}{s} + \frac{\sin^4\beta(s)}{s} - 2k_2 q_0 s\beta'(s) + k_2 s\beta'^2(s) \right] \\ + \frac{1}{2}\big(k_2 - k_{24} + k_2 q_0^2 - (k_2 - k_{24})\cos 2\beta(1)\big), \end{aligned} \tag{A4}$$

when $\beta(0)$ is 0 required by the symmetry. Minimizing the functional of the form,

$$f = \int_0^1 ds\, \mathrm{L}[\beta(s), \beta'(s), s] + \mathrm{K}[\beta(1)], \tag{A5}$$

where $\beta(0)$ is fixed as 0 and $\beta(1)$ is free, we calculate the following stationary of the integral,

$$0 = \delta f = \int_0^1 ds \left(\frac{\partial \mathrm{L}}{\partial \beta} - \frac{d}{ds}\frac{\partial \mathrm{L}}{\partial \beta'} \right) \delta\beta + \left(\frac{\partial \mathrm{L}}{\partial \beta'} + \frac{\partial \mathrm{K}}{\partial \beta} \right)\Big|_{s=1} \delta\beta(1). \tag{A6}$$

Setting the coefficients of $\delta\beta$ and $\delta\beta(1)$ to 0 gives the Euler-Lagrange equation and the boundary condition, respectively. The Euler-Lagrange equation is

$$0 = \frac{\partial \mathrm{L}}{\partial \beta} - \frac{d}{ds}\frac{\partial \mathrm{L}}{\partial \beta'} = -2k_2 q_0 s \cos 2\beta(s) + \frac{k_2 \sin 4\beta(s)}{2} + 4\sin^3\beta(s)\cos\beta(s) - (-2k_2 q_0 s + 2k_2 s\beta'(s) + 2k_2 s^2\beta''(s)), \tag{A7}$$

which simplifies to

$$s^2\beta''(s) + s\beta'(s) - \frac{\sin 2\beta(s)\cos 2\beta(s)}{2} - \frac{2\sin^3\beta(s)\cos\beta(s)}{k_2} + s q_0(\cos 2\beta(s) - 1) = 0. \tag{A8}$$

The boundary condition in addition to $\beta(0) = 0$ is

$$0 = \left(\frac{\partial \mathrm{L}}{\partial \beta'} + \frac{\partial \mathrm{K}}{\partial \beta} \right)\Big|_{s=1} = -2k_2 q_0 - (k_{24} - k_2)\sin 2\beta(1) + 2k_2\beta'|_{s=1}, \tag{A9}$$

which is equivalent to

$$\beta'|_{s=1} = q_0 + \frac{(k_{24} - k_2)}{2k_2} \sin 2\beta(1). \tag{A10}$$

Note that, as shown in Davidson *et al.*, Eqs. (A8) and (A10) can be solved analytically to give Eq. (1) when $q_0 = 0$, i.e., no chiral dopant [29].

[1] H. Coles and S. Morris, Nat. Photonics **4**, 676 (2010).
[2] J. Beeckman, K. Neyts, and P. Vanbrabant, Opt. Eng. **50**, 081202 (2011).
[3] J. Ortega, C. Folcia, and J. Etxebarria, Materials **11**, 5 (2017).
[4] A. N. Bogdanov, U. K. Rößler, and A. A. Shestakov, Phys. Rev. E **67**, 016602 (2003).
[5] J. Fukuda and S. Žumer, Nat. Commun. **2**, 246 (2011).
[6] A. O. Leonov, I. E. Dragunov, U. K. Rößler, and A. N. Bogdanov, Phys. Rev. E **90**, 042502 (2014).
[7] C. Melcher, Proc. R. Soc. London A **470**, 20140394 (2014).
[8] P. J. Ackerman, J. Van De Lagemaat, and I. I. Smalyukh, Nat. Commun. **6**, 6012 (2015).
[9] L. Cattaneo, Ž. Kos, M. Savoini, P. Kouwer, A. Rowan, M. Ravnik, I. Muševič, and T. Rasing, Soft Matter **12**, 853 (2016).
[10] Y. Guo, S. Afghah, J. Xiang, O. D. Lavrentovich, R. L. B. Selinger, and Q.-H. Wei, Soft Matter **12**, 6312 (2016).
[11] G. De Matteis, L. Martina, and V. Turco, Theor. Math. Phys. **196**, 1150 (2018).
[12] J. Fukuda, A. Nych, U. Ognysta, S. Žumer, and I. Muševič, Sci. Rep. **8**, 17234 (2018).
[13] J. Bezić and S. Žumer, Liq. Cryst. **14**, 1695 (1993).
[14] A. Kilian and A. Sonnet, Phys. Rev. E **52**, 2702 (1995).
[15] H.-S. Kitzerow, B. Liu, F. Xu, and P. P. Crooker, Phys. Rev. E **54**, 568 (1996).
[16] M. Ambrozic and S. Zumer, Phys. Rev. E **54**, 5187 (1996).
[17] M. Ambrožič and S. Žumer, Phys. Rev. E **59**, 4153 (1999).
[18] L. Tortora and O. D. Lavrentovich, Proc. Natl. Acad. Sci. USA **108**, 5163 (2011).
[19] C. Peng and O. D. Lavrentovich, Soft Matter **11**, 7257 (2015).
[20] A. Darmon, O. Dauchot, T. Lopez-Leon, and M. Benzaquen, Phys. Rev. E **94**, 062701 (2016).
[21] A. Darmon, M. Benzaquen, S. Čopar, O. Dauchot, and T. Lopez-Leon, Soft Matter **12**, 9280 (2016).
[22] J. Ignés-Mullol, G. Poy, and P. Oswald, Phys. Rev. Lett. **117**, 057801 (2016).
[23] T. Ogolla, S. B. Nashed, and P. J. Collings, Liq. Cryst. **44**, 1968 (2017).
[24] L. Tran, M. O. Lavrentovich, G. Durey, A. Darmon, M. F. Haase, N. Li, D. Lee, K. J. Stebe, R. D. Kamien, and T. Lopez-Leon, Phys. Rev. X **7**, 041029 (2017).
[25] T. Shirai, M. Shuai, K. Nakamura, A. Yamaguchi, Y. Naka, T. Sasaki, N. A. Clark, and K. V. Le, Soft Matter **14**, 1511 (2018).
[26] T. Ogolla, R. S. Paley, and P. J. Collings, Soft Matter **15**, 109 (2019).
[27] O. D. Lavrentovich, Phys. Rev. A **46**, R722 (1992).
[28] J. Jeong, Z. S. Davidson, P. J. Collings, T. C. Lubensky, and A. G. Yodh, Proc. Natl. Acad. Sci. USA **111**, 1742 (2014).
[29] Z. S. Davidson, L. Kang, J. Jeong, T. Still, P. J. Collings, T. C. Lubensky, and A. G. Yodh, Phys. Rev. E **91**, 050501(R) (2015).
[30] K. Nayani, R. Chang, J. Fu, P. W. Ellis, A. Fernandez-Nieves, J. O. Park, and M. Srinivasarao, Nat. Commun. **6**, 8067 (2015).
[31] J. Jeong, L. Kang, Z. S. Davidson, P. J. Collings, T. C. Lubensky, and A. G. Yodh, Proc. Natl. Acad. Sci. USA **112**, E1837 (2015).
[32] K. Nayani, J. Fu, R. Chang, J. O. Park, and M. Srinivasarao, Proc. Natl. Acad. Sci. USA **114**, 3826 (2017).
[33] J. Fu, K. Nayani, J. O. Park, and M. Srinivasarao, NPG Asia Materials **9**, e393 (2017).
[34] A. Javadi, J. Eun, and J. Jeong, Soft Matter **14**, 9005 (2018).
[35] H. Lee and M. M. Labes, Mol. Cryst. Liq. Cryst. **84**, 137 (1982).
[36] C. K. McGinn, L. I. Laderman, N. Zimmermann, H.-S. Kitzerow, and P. J. Collings, Phys. Rev. E **88**, 062513 (2013).
[37] A. A. Joshi, J. K. Whitmer, O. Guzmán, N. L. Abbott, and J. J. de Pablo, Soft Matter **10**, 882 (2014).
[38] Ž. Kos and M. Ravnik, Soft Matter **12**, 1313 (2016).
[39] S. Zhou, K. Neupane, Y. A. Nastishin, A. R. Baldwin, S. V. Shiyanovskii, O. D. Lavrentovich, and S. Sprunt, Soft Matter **10**, 6571 (2014).
[40] N. Zimmermann, G. Jünnemann-Held, P. J. Collings, and H.-S. Kitzerow, Soft Matter **11**, 1547 (2015).
[41] V. Koning, B. C. van Zuiden, R. D. Kamien, and V. Vitelli, Soft Matter **10**, 4192 (2014).
[42] T. Mori, A. Sharma, and T. Hegmann, ACS Nano **10**, 1552 (2016).
[43] A. Nemati, S. Shadpour, L. Querciagrossa, L. Li, T. Mori, M. Gao, C. Zannoni, and T. Hegmann, Nat. Commun. **9**, 3908 (2018).
[44] V. R. Horowitz, L. A. Janowitz, A. L. Modic, P. A. Heiney, and P. J. Collings, Phys. Rev. E **72**, 041710 (2005).
[45] J. Ding and Y. Yang, Jpn. J. Appl. Phys. **31**, 2837 (1992).